4D Fabrication of Polymers for Deployable Medical Devices

Introduction:

The field of additive manufacturing has progressed rapidly making huge strides in various sectors, including automobiles, food and pharmaceuticals, soft robotics, and medicine. It has especially benefitted the medical devices sector, allowing for easy customization and scalability. However, conventional three-dimensional (3D) printing is often difficult to be employed for creating complex shapes. Four-dimensional (4D) printing is trending in the rapidly growing field of additive manufacturing with the prospect of impact in several domains, including healthcare[1-2]. This emerging technology enables the fabrication of complex and dynamic structures, which are otherwise difficult to realize using conventional three-dimensional (3D) printing[3-4]. 4D printing utilizes either smart materials that respond to specific stimuli[5-6], programmed design during printing[7-8], or a combination of both[9-11]. There is a wide range of smart materials that respond to stimuli[12-13], such as changes in pH[14-15], temperature[16], light[17-18], moisture[19-20], magnetic field[21-22], etc. In recent years, the rapid advancements in tissue engineering combined with an expanded choice of biomaterials have motivated research in 4D printing for regenerative medicine[23-25]. However, the fabrication of complex constructs that faithfully mimic tissue architecture persists as a challenge. Hydrogels are the ideal candidates for engineering tissue scaffolds[26-27], owing to their biocompatibility, high water-absorption capacity, and chemical tunability. Nevertheless, the choice of hydrogels for 4D printing is rather limited owing to their poor printability and shape fidelity and the limited choice of stimuli that are physiologically relevant while exhibiting good biocompatibility[28-29]. Moreover, controlling the time-scale and tendency of deformation is often challenging, as it necessitates smart design[30]. A critical limitation of 3D printing is the static nature of the fabricated hydrogels, requiring surgical implantation[31]. This strategy demands inconvenient surgical sutures that are often accompanied by complications, including additional traumatic damage and severe inflammation around the injured tissue[32]. 4D printing offers a promising route to generate dynamic shape-morphing geometries out of static parts while leveraging the benefits of near-near-net-shape manufacturing of complex and patient-specific parts. Target designs are encoded during the printing process, which govern the resulting shape deformations post-printing. Hydrogels can swell in response to water uptake and hence, are the material of choice by researchers developing 4D printed biomaterials. Few recent studies report shape deformations of hydrogels, primarily governed by anisotropic swelling, gradients in cross-linking densities, etc. However, their applications *in vivo* are limited due to poor control on programming specific shape deformations in constructs prepared from a single material [28, 33], the prolonged time required for the deformations[29], complex bioink preparation[34], and poor control on processes to impart anisotropy within the materials[35-37], etc. These drawbacks hinder the widespread adoption of 4D printed gels for applications necessitating intraoperative shape deformations of deployable devices in minimally-invasive procedures. *In vivo* 3D printing of scaffolds for tissue regeneration has been demonstrated[38], but 4D printed hydrogels with *in vivo* shape-morphing ability are yet to be realized. Among several potential biomedical

applications, self-folding nerve conduits that alleviate tedious suturing could benefit the large patient population requiring microsurgeries for nerve repair[39].

The other class of polymers, namely thermoplastics are mostly used for hard tissue regeneration owing to their excellent mechanical properties and tunable degradation rates. In order to facilitate in situ deployment of scaffolds, smart materials used are typically shape-memory polymers (SMPs), which exhibit the unique property of stabilizing a temporary deformed shape and subsequent recovery back to their original shape by the application of an external stimulus[40]. This property stems from the distinct molecular architectures of the polymers. The presence of such distinct phases in the polymer allows it to be fixed into a temporary shape by deformation (governed by netpoints or hard segments) below the transition temperature, followed by recovery into original shape (influenced by molecular switches or soft segments) upon heating it above the transition temperature. In the field of biomedicine, it is also essential that the SMP being used is biocompatible and preferably biodegradable. Polylactide-co-trimethylene carbonate (PLMC), a biodegradable polymer, has been explored as a versatile shape memory polymer in some studies for biomedical applications[41]. The distinct advantage is its glass transition temperature (Tg), which lies close to the physiological temperature, rendering it a promising candidate for in vivo applications. However, triggering shape recovery through direct heating is not feasible in many cases, particularly for in vivo applications requiring intraoperative stimulation. Thus, athermal heating, which is possible by careful selection of the nanofillers incorporated in the polymer matrix, is a potentially viable means of exploiting the shape memory materials for remote actuation. The stimulus could be light, ultrasound, water, microwaves, etc. Magnetic stimulation is a potential means of remote actuation of these materials via indirect heating. The most popular nanofiller in this regard is iron oxide (Fe_3O_4) nanoparticles which have an excellent inductive heating ability. Fe_3O_4 nanoparticles have far-reaching applications in biomedicine, including hyperthermia for cancer treatment, magnetic resonance imaging contrast agents, etc. These nanoparticles also have the ability to transfer energy from the radio-frequency field to surrounding media via heat dissipation.

As bone tissues are among the most widely transplanted tissues, there is significant demand for engineering tissue scaffolds for the repair and regeneration of bony tissues. In the clinic, remotely deployable scaffolds could facilitate minimally-invasive procedures. Similarly, deployable scaffolds can self-fit into complex, irregular defects. For clinical success, the SMP and its composite should effectively promote osteogenesis. There are only a few reported examples of smart biomaterials for bone tissue regeneration, such as inductive heating responsive-PLA/ Fe_3O_4 composites[42], electroactive PLA-aniline trimer[43], and PCL (poly ε caprolactone) diacrylate-based SMP[44]. However, these reported SMPs either require extensive chemical synthesis to fabricate or are not amenable to advanced techniques of manufacturing, such as 3D printing. Most of the SMPs also have markedly higher Tg than physiological levels, which risks inducing thermal necrosis of surrounding tissues, if deployed in vivo. So far, there are few examples of studies that demostrate SMP composites with remote heating capability

near body temperature while concurrently promoting osteogenesis, which can thereby enable the in situ triggering of shape change for self-fitting bone scaffolds.

Objectives:

1. **Moisture responsive hydrogels for soft tissue regeneration**
   - Fabrication of gel with differential properties
   - Design-assisted 3D printing
   - Characterization of gels for extrusion printing, mechanical and physico-chemical properties
   - Biocompatibility of the gels
   - Application of self-rolling gels as sutureless nerve guidance conduits (NGCs)
   - *In vivo* neural regeneration facilitated by NGCs

2. **Shape Memory polymer composites for hard tissue regeneration**
   - 3D printing of magnetic particle reinforced SMPs
   - Mechanical and shape memory characterization
   - Biological characterization
   - *In vitro* osteogenic potential
   - *In vivo* biocompatibility

Materials and Methods

1. **Moisture responsive hydrogels for soft tissue regeneration**

Gel preparation

The hydrogels were prepared as reported previously with modifications. Briefly, for preparing the Alg/MC:3/9 hydrogels, 3% (w/v) alginic acid sodium (Alg; Sigma Aldrich) was added to 4 ml of deionized (DI) water with constant stirring at 60⁰C to obtain a clear solution. Next, 9% (w/v) MC (Viscosity 4000 cP; Sigma Aldrich) was added slowly with continuous stirring at 60⁰C until MC dissolved completely, and a homogenous solution was obtained. The resulting solution was then filled in a cartridge used for 3D printing and was kept at 4⁰C for 30 min for complete hydration of MC, following which the cartridge was stored at room temperature (RT, 25⁰C) until further use. For preparing the Alg/MC:4/6 gels, a similar procedure was adopted with 5 mM $CaCl_2$ solution as the medium.

Gel characterization

The pore morphology of both the gels (Alg/MC:3/9 and Alg/MC:4/6) was characterized using a scanning electron microscope (SEM, JEOL iT 300). The gels were lyophilized and sputter-coated with gold before observation. Swelling studies were performed after drying the gels overnight. The initial dry weight (W0) of the gels was measured and then soaked in 200 mM

CaCl2 solution. The weight (Wt) of the gels was monitored at regular intervals. The extent of swelling was calculated using the equation:

Swelling (%) = (Wt-W0)/Wt×100

The viscoelasticity of the gels was characterized using a rotational rheometer (Anton Paar Modular Compact Rheometer- 302) with a 10 mm parallel plate and 1 mm gap. For the viscosity flow test, the viscosity of the gels was measured at shear rates ranging from 1 to 100 s-1. For the angular frequency sweep, a constant strain of 1% was chosen from the linear viscoelastic region (LVR), and angular frequency was varied from 1 to 100 rad s-1. Thixotropy characterization was performed in three steps: a low shear rate of 0.1 s-1 was applied to the gels for 60 s, the shear rate was increased to 100 s-1 for 10 s, and finally, the shear rate was lowered to 0.1 s-1 for 60 s.

Finite Element Analysis (FEA) theory and simulations

Different 3D models were prepared in Solidworks (Dassault Systems), which were then imported into the commercially available FEA software package Abaqus 2017 (Simulia 2017) to predict the deformation of the hydrogel designs experimentally.

4D printing of multi-component hydrogels

To enable the process of 4D printing, the 3D models were designed in Solidworks (Dassault System), which were converted to StereoLithography (.Stl) format for slicing to generate G-codes (Repetier Host, Cellink). For creating the G-codes, the print paths were defined as per computational designs, wherein a first solid layer of Alg/MC:3/9 was overlaid by stripes of Alg/MC-4/6 placed at different angles on the second and third layers with respect to the first layer. For creating stripes, 40% aligned rectilinear infill patterns with defined fill angles were used, as per computational design. The resulting G-codes were then input to an extrusion-based 3D bioprinter (BioX, Cellink) for 3D printing of the gels independently from two nozzles. The printed constructs were air-dried for 8 h at RT and immersed in 200 mM CaCl2 solution. The resulting shape changes were recorded digitally

In vivo studies on the sciatic nerve transected model

Precisely, adult Sprague-Dawley male rats (between 250-270 grams at the time of surgery) were selected to estimate the efficacy of fabricated scaffolds in the regeneration of PNS involving the earlier described sciatic nerve injury model, as described earlier60. A total of 16 animals were arbitrarily divided into four groups - sham-operated (operational control), negative control (injury without any treatment given), uncoated (4D printed rectangular sheets without any fibers coating), and coated (4D printed rectangular sheets with fibers coating). The resulting dimensions of the self-folding sheets were calculated using simulations to yield conduits to sufficiently cover the defect. Each group contained four animals. Sciatic nerve regeneration was investigated in this work using an injury model with a 2 mm transection. Both the coated and uncoated sheets were sterilized through UV irradiation. Before transplantation, the sheets, including coated and uncoated, were stimulated with 200 mM of CaCl2 solution and placed at the defect site. Thereafter, 5 mM CaCl2 was poured over the sheets to induce self-folding into tubular structures spontaneously around the injured nerve due to the pre-

programmed deformation. Intraperitoneal injections of ketamine (90 mg/kg) and xylazine (10 mg/kg) were used to anesthetize the animals, followed by a bilateral incision at the left lateral thigh. The sciatic nerve was uncovered by cutting through the bicep femoris and gluteus superficialis muscles. Each rat had a 2 mm nerve deficit, which was then bridged utilizing different neural scaffolds. Nerve conduits were used to connect the proximal and distal ends of the damaged nerve. As the conduits were wrapped automatically around the wound, thus no suturing was required. A 2-mm segment of the sciatic nerve was removed, and the two ends were left untreated for the negative group. The muscle and skin layers were appropriately sutured with 30 nylon sutures after the implant site had been cleaned and disinfected. To avoid infection, each rat was administered 800,000 units of penicillin immediately following surgery.

Behavioral Studies:

Functional recovery tests

The functional recovery of the animals was assessed at 1st, 15th, 30th, and 45th days post-operatively using the hot plate test and Randall-Selitto test to assess thermal reactivity and mechanical threshold, respectively. For thermal reactivity assessment, each rat was individually placed on a metal hot plate of 30 x 30 cm held at 45±1 °C. The frequency with which the left paw was lifted in order to balance the weight on the right paw, which was not damaged, was carefully observed as a reaction to thermal allodynia. The lifting of paws as a result of regular movement was disregarded[60].

The Randall-Selitto paw pressure test was performed using an analgesy meter. Increasing mechanical pressure was administered to the experimental rat leg on the medical section of the plantar surface of the left hind paws as late as observing a withdrawal response. For each animal, the amount of pressure that caused a withdrawal reaction was recorded.

Sciatic Functional Index (SFI)

SFI was determined from this formula:

SFI = −38.3 × (EPL−NPL)/NPL + 109.5 × (ETS−NTS)/NTS

+13.3 × (EIT−NIT)/NIT−8.8

Where PL indicates the footprint length, TS denotes the total toe spread, IT stands for intermediate toe spread, E is the injured side, and N represents the distance on the contralateral side[61]. Scheme 1 represents the schematic diagram of the paw indicating PL, TS, and IT for a better understanding.
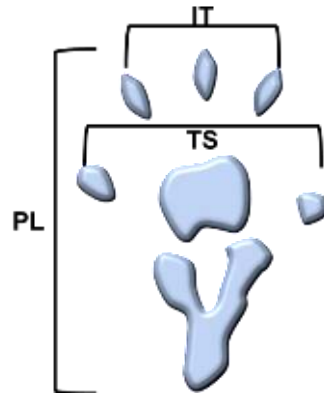
Scheme 1. Schematic diagram of paw indicating the PL, TS and IT.

Tissue Collection

The animals were sacrificed after six weeks post-implantation via dislocation of the cervical vertebrae to harvest the tissues. The surgical site was opened up to isolate the scaffold-wrapped area of the resected sciatic nerve in each rat. After separation, the nerve conduits containing the regenerated neural tissues were fixed with 10% neutral-buffered formalin (NBF) at RT for 24 h. The fixed tissues were used for immunohistochemistry (IHC) and H&E staining. Gastrocnemius muscles of operated left legs were collected for wet weight measurement and HE staining.

H&E and IHC Staining

Six weeks post-implantation, the regenerated nerves in the conduits were examined histologically. 5 μm thick longitudinal and cross sections were cut from the fixed samples using a microtome (Leica) and embedded in paraffin wax. The sections were deparaffinized with xylene and with a gradient of diluted ethanol (100, 90, 70, and 50%). They were further rehydrated, which was followed by gentle rinsing in tap water and stained with freshly prepared HE62. The sections were dried and mounted on coverslips in DPX (di-styrene, a plasticizer, and xylene) (SRL, India). A microscope with RGB (Red, Green, Blue) filters (Lionheart LX, BioTek, USA) was used to image the stained sections to observe the morphology of regenerated nerve tissues.

Immunofluorescence was performed on cross-sections and longitudinal sections taken from the central portion of the regenerated tissues in the conduit after staining for NF200 and S-100. The procedure described above for IHC staining was used. After rehydration, antigen retrieval was carried out by incubating for 3 min under moist pressure in sodium citrate buffer (pH 6). After rinsing in Tris-buffered saline (pH 7.6), the sections were dried. 1% BSA was used for 2 h as a blocking agent, followed by overnight incubation with mouse monoclonal NF-160 (Sigma-Aldrich, USA) and rabbit polyclonal S100 (Invitrogen, USA) at 4°C. The sections were washed with Tris-buffered saline containing 0.1% Tween® 20 Detergent (TBST) and incubated with rabbit anti-mouse IgG (H + L) − fluorescein isothiocyanate conjugate (Thermo, USA) secondary antibody for NF-160 and the goat antirabbit IgG (H + L) −tetramethylrhodamine isothiocyanate conjugate (Thermo, USA) secondary antibody for S100 for 2 h followed by washing with TBST. The sections were counterstained with DAPI (HiMedia). Finally, the

samples were observed using an epi-fluorescence microscope (Lionheart LX, BioTek, USA). At least three areas were sampled for each section/group.

2. Shape Memory polymer composites for hard tissue regeneration

Fabrication and 3D printing of PLMC-Fe3O4 nanocomposites

PLMC was dissolved in DCM (0.15 g/mL) under continuous magnetic stirring till a clear homogeneous solution was obtained. Fe3O4 nanoparticles were sonicated in DCM using probe sonication for about 40 min till a well-dispersed suspension was obtained. The suspension was then transferred into the polymer solution, and the resulting solution was further bath sonicated for another 40 min for the particles to homogeneously disperse in the polymer matrix. This solution was then cast over Teflon sheets and left to dry overnight. The composite film, obtained upon drying of the solvent, was then kept inside a vacuum oven for about 48 h to completely remove any traces of solvent present in the film. The obtained film was chopped into smaller uniform pieces and fed inside the metal cartridge of the 3D printer (BioX, CELLINK). Thermoplastic print head of the printer was used to facilitate melt-extrusion of the composites.

Printing parameters were optimized to get good accuracy and resolution of the composite structures. Printing temperatures were in the range of 200°C to 210°C, the pressure of about 200 kPa, and printing speed ranging between 4 and 6 mm/s, depending on the complexity of the structures.

Thermal characterization

The thermal properties of the polymer and nanocomposite were characterized using a differential scanning calorimeter (DSC, TA Instruments Q 2000). The samples of weight 3-5 mg were scanned between -70°C and 200°C at a scanning rate of 10°C min-1. The samples were subjected to a heat-cool-heat cycle to remove any processing history. Thermal degradation was performed on the samples using a thermogravimetric analyzer (TGA, TA Instruments Q 500). Samples of 3-5 mg were heated from 40°C to 800°C at a heating rate of 10 °C min-1 under an inert atmosphere.

Shape-memory characterization

Shape memory properties of both the 3D printed polymer and composite structures were assessed by performing a shape memory testing cycle using TA instruments-Q800, Dynamic Mechanical Analysis (DMA). The samples for this test were prepared by 3D printing the materials into rectangular strips of 25×6×1 mm3. The test was performed in stress-controlled tension mode in the following program:

i) Deformation: The printed sample was heated to a temperature Td (deformation temperature slightly above Tg) and equilibrated for 5 min with a preload of 0.005 N, which gives the initial strain ($\varepsilon_{initial}$). The sample was then stretched isothermally from 0.001 to 0.025 MPa with a stress ramp rate of 0.005 MPa/min. The strain at this point was denoted as deformed strain ($\varepsilon_{deformed}$).

ii) Cooling: The sample was then cooled to 0°C (much below Tg) at a rate of 5°C min-1. It was equilibrated for 5 min under the application of constant stress.

iii) Fixing: The external stress was unloaded isothermally at a rate of 0.005 MPa/min. It was again equilibrated at 0°C for 5 min, and the strain captured at this point was fixed strain (εfix).

iv) Recovery: The sample was reheated at a rate of 5°C min-1 to Td and equilibrated for 10 min. The recorded strain is indicated as the residual strain after recovery (εrecov). The sample was finally cooled down to 0°C.

Morphological and chemical characterization

Fe3O4 nanoparticles were characterized for their morphology and chemical structure using a scanning electron microscope (Ultra 55 FESEM, Karl Zeiss Mono) and X-ray diffractometer (XRD), respectively. The particles were dispersed homogeneously in ethanol before drop casting over silicon wafers, which were mounted on an aluminum stub, sputter coated with gold, and then imaged under SEM. An accelerating voltage of 4 kV and a secondary electron detector (SE2) was used.

PLMC- Fe3O4 composites were 3D printed into disc-shaped structures, desiccated, and gold-sputtered before visualization under SEM. PLMC and PLMC- Fe3O4 composites were characterized for chemical structure using Fourier transform infrared spectroscopy - attenuated total reflectance (FTIR-ATR) analysis on a Perkin Elmer Fourier spectrometer, USA. The spectra were recorded in the range of 650-400 cm-1 with a resolution of 4 cm-1.

Magnetic field heating of PLMC-Fe3O4 nanocomposites

Magnetic hyperthermia heating was achieved by using the Ambrell Easyheat Induction system (10 kW). The magnetic field generated inside the coil was kept at 40 kA m-1 (500 Gauss). The magnetic field oscillated at a frequency of 215 kHz. The power delivered at the center of the hyperthermia coil was kept in the range of 3.7 kW to 4.1 kW.

In vitro cytocompatibility

NIH-3T3 cells were cultured in DMEM high glucose cell culture media (supplemented with 10% FBS). Sterilized samples were then seeded with fibroblast cells (NIH-3T3) at 8-10 passages at a density of 10,000 cells/cm2. Cell growth was monitored using Alamar blue assay following the manufacturer's protocol (Thermo Fisher Scientific, USA). Cells at day 3 post seeding were also stained with Calcein-AM/ Ethidium homodimer (EtDi, EthD-1; Thermo-fisher scientific, USA) to visually analyze the toxicity of prepared samples. Morphology of seeded cells was also analyzed on Days 3 and 5 using Phalloidin (Alexa fluor 488, Thermo Fisher Scientific, USA)/DAPI (4′,6-diamidino-2-phenylindole, Thermo Fisher Scientific, USA) double staining.

Osteogenic potential assessment

MC3T3-E1 mouse calvarial pre-osteoblasts were cultured in α-minimum essential medium (α-MEM) containing 10 vol.% fetal bovine serum. The 3D printed scaffolds were UV-sterilized

before seeding cells on them at a density of 7000 cells/cm2. Cells on the scaffold surface were evaluated by Live/Dead assay 24 h post-seeding to qualitatively assess the viability of the seeded cells. The F-actin arrangement in the cells was evaluated by actin and nuclear staining after 24 h. The seeded cells were first fixed with 3.7% formaldehyde. 0.1% Triton X-100 was used to permeabilize the cells. The samples were incubated with the Phalloidin/ DAPI (6.6 µM phalloidin and 1 µg/mL DAPI) for 15 min before imaging with an epi-fluorescence microscope.

For assessing osteogenesis in vitro, 24 h post-seeding of the cells in growth medium (complete culture medium as described above), the medium was replaced with osteogenic medium (growth medium containing 10 nM dexamethasone, 50 µm ascorbic acid, and 10 mM β glycerophosphate, all Sigma Aldrich). The mineral deposition was assessed on days 7 and 14 with Alizarin red S (ARS, Sigma) dye which binds to the calcium salts. Cells were fixed in formaldehyde, and the samples were incubated in 2% ARS solution for 40 min. The scaffolds were washed with ultrapure water and incubated in 5% sodium dodecyl sulfate (SDS) solution in 0.5 N HCL solution for 45 min. The absorbance of the dissolved stain was quantified at 405 nm using a microplate reader.

In vivo biocompatibility assessment

The in vivo toxicity of the scaffolds was assessed using Wistar rats. All the animal work was performed in accordance with 86/609/EEC act and approved by the Institute Animal Ethics Committee of the Indian Institute of Science, Bangalore (protocol number CAF/Ethics/878/2022). Adult male Wistar rats aged 8-10 months, weighing 190–230 g, were housed in well-ventilated cages supplied with autoclaved sawdust beddings. Food and sterile water were given ad libitum. 12 h light and dark cycle was maintained in the animal house at 25 ± 1 °C with 55±5% humidity. The surgeries and experiments were performed in the light cycle. The animals were divided into three groups, i.e., sham, PLMC, and composite scaffolds, with each group containing three animals. All the animals were anesthetized on day 15 by injecting a cocktail of 80 mg/kg ketamine and 15 mg/kg xylazine intraperitoneally. The coat around the mid-dorsal area of anesthetized animals was shaven and sterilized with betadine, and a horizontal incision of approximately 1.5 cm was made in the skin with a sterile surgical blade to create a subcutaneous pocket. UV sterilized scaffolds were implanted inside the subcutaneous pocket, and the incision was closed with 4.0 sutures. No implantation was done in sham control rats. At the end of 15 days, the animals were sacrificed, and the skin tissue around the implant site was excised and preserved in formalin solution (10% in PBS). Vital organs, such as the kidney and liver, were also taken out for evaluation and preserved in the formalin solution. The fixed tissue was then embedded in paraffin, and tissue sections of 5 µm were prepared by microtome. The obtained sections were stained with hematoxylin and Eosin (H&E) and imaged under a light microscope (IX-53, Olympus).

To assess any inflammatory response, hematological parameters were also checked. On day 7 and day 15, 1 ml of blood was collected from each animal. The blood was collected in heparin-coated tubes for the estimation of Total Leukocyte Count (TLC), Erythrocyte Sedimentation Rate (ESR), Serum glutamic pyruvic transaminase (SGPT) and Serum Glutamic-Oxaloacetic Transaminase (SGOT).

Statistical analysis:

The results are presented as mean ± standard error for each group. GraphPad Prism 5.04 was used for the statistical analysis (GraphPad Software, USA). One-way ANOVA was used for the statistical analysis, which was then followed by Dunnett and Tukey tests for significance. All analyses were carried out at 95% confidence level and were considered to be significant at statistical probability (p-value) <0.05. Statistical significances were denoted as (*/#/@), (**/##/@@) and (***/###/@@@) for $p < 0.05$, $p < 0.01$ and $p < 0.001$, respectively.

Results and discussion

A dual-component hydrogel system was utilized in this work. Two formulations of A/MC were prepared with different fractions of A and MC such that one resulting gel (A/MC: 3/9 by mass prepared in DI water) exhibited a higher swelling rate, and the other (A/MC: 4/6 in 5 mM $CaCl_2$ solution) exhibited a relatively lower swelling rate. These compositions were identified after careful evaluation of the printability and swelling rates of several formulations. The physicochemical properties of the individual gels were characterized initially. Morphological analysis by scanning electron microscopy (Figure 1a) revealed that the gels were highly porous with interconnected pores. Notably, A/MC:3/9 contained bigger pores than A/MC:4/6, as evident from the cross-sectional SEM micrographs in Figure S2. This trend corroborates the swelling measurements (Figure 1b), which show that A/MC:3/9 swells considerably more than A/MC:4/6.

Rheological characterization to assess the printability and viscoelastic behavior of the gels confirmed the shear thinning behavior of both hydrogels (Figure 1c), rendering them suitable for extrusion-based 3D printing. Figure 1d reveals the viscoelastic properties of the gels with the storage moduli values higher than loss moduli in the entire linear viscoelastic (LVR) region. Figure 1e shows that the gels were thixotropic such that the viscosities of both the gels decrease under high shear rates and consequently recover to the original values upon releasing the stress. This property endows the gels with good printing fidelity and is a consequence of chain disentanglements and re-entanglements simultaneously under high and low shear rates, respectively.
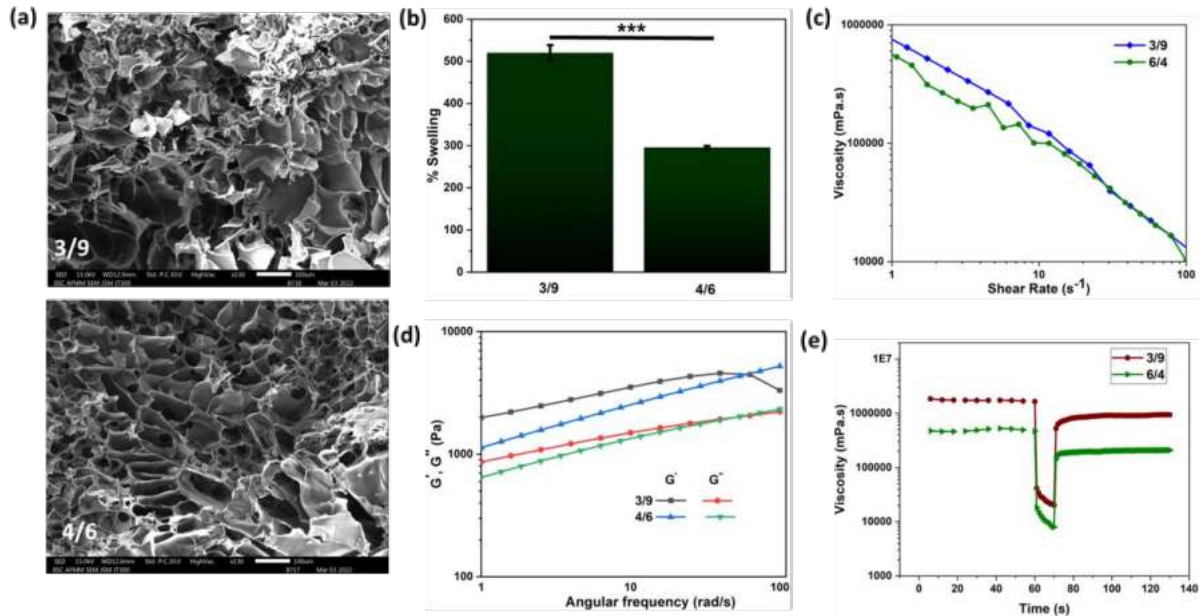
Figure 1: Characterization of the A/MC: 3/9 and 4/6 hydrogels. (a) SEM image revealing that both gels are porous (*Scale bars are 100 µm*); (b) Swelling ratios for the two gels; (c-e) Rheological analysis of the gels; (c) Shear-thinning behavior, (d) Viscoelastic properties of the two gels, and (e) Thixotropic properties of the two gels. (*** denotes p<0.001).

A computational model was formulated to reliably predict the different shape deformations of the 3D printed structures with defined infill patterns. At first, the effect of the topography of the top layer on the shape deformation was evaluated by designing a simple tri-layered trapezoidal geometry. The first layer was a solid base material of higher expansion coefficient, which was decorated with stripes of the second material of lower expansion coefficient placed precisely at different orientations with respect to the base layer (Figure 2a (i - iii)). The expansion coefficients for the two materials were calculated from the swelling ratios of the two gels. FEA (finite element analysis) simulations (Figure 2a (iv - vi)) revealed that a trapezoid could deform remarkably differently for the varied arrangements between the two layers, namely, bending along the longer axis for stripes placed parallel (or at 0°) with respect to the long axis of the base layer, twisting for stripes at 45°, and bending along the shorter axis for stripes at 90°. An extrusion-based 3D printer with two nozzles for the two gel formulations was used to print the gels following these G-codes for three different designs. The printed structures were air-dried for 8-10 h and subsequently swelled in 200 mM $CaCl_2$ solution to initiate the shape deformation.
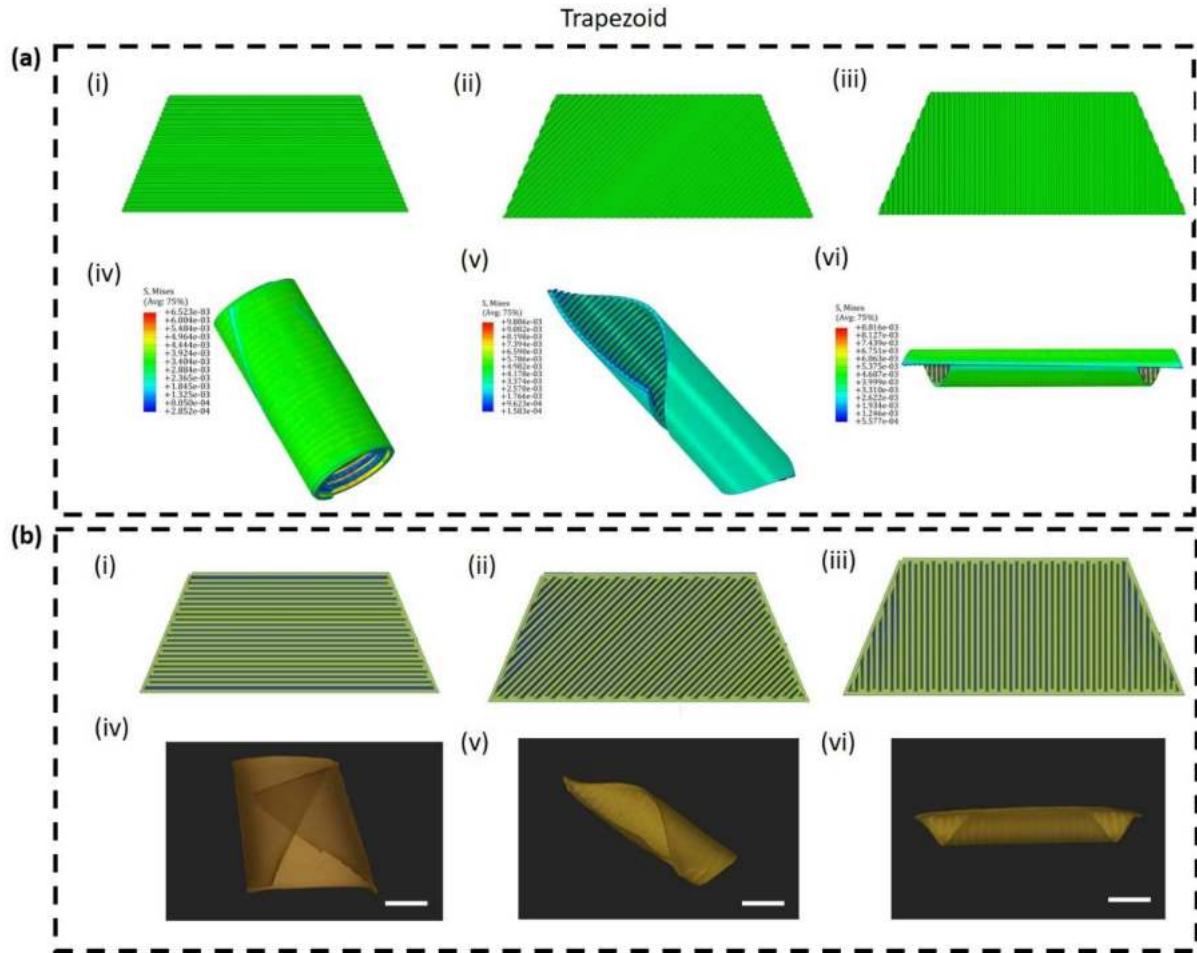
Figure 2: FEA simulations and experimental validation of shape deformations. (a) Computational analysis wherein i, ii, and iii are the modeled geometries and iv, v, and vi are the corresponding simulated deformations. (b) Experimental validation wherein i, ii, and iii are the modeled G-codes and iv, v, and vi represent the digital photographs of the deformed gels. *Scale bars: 12 mm*

We confirmed that our hydrogels (both uncoated and nanofiber-coated gels, hereafter termed uncoated and coated, respectively) were biocompatible *in vitro* and *in vivo* and that nanofibers do not impact shape deformation. Next, we aimed to demonstrate the clinical benefit of the shape-changing 4D printed hydrogel focusing on its utility as sutureless NGCs. Toward this goal, rectangular models were designed for fabrication by 3D printing to self-roll into tubular constructs of predetermined dimensions upon stimulation with $CaCl_2$ solution. Thus, the self-rolled gel matches the biomechanics of soft tissues and is well suited for engineering NGCs.

Several artificial conduits for nerve regeneration have been developed, some of which have been approved for clinical use by the Food and Drug Administration (FDA). In both preclinical and clinical trials, the single tubular structure, NeuraGen and Neurolac, derived from type I collagen and PCL, respectively, showed promising outcomes. However, both of these commercially-available conduits require suturing. Even though sutures are widely accepted as the standard therapy for peripheral nerve injury (PNI), they are not without risk, including further traumatic injury and severe inflammation surrounding the wounded nerve tissues,

preventing effective regeneration of the nerve. Hence, in an attempt to establish a rapid and efficient neurorrhaphy treatment for improving prognosis without any severe inflammatory complications, the 4D printed conduit designed in this study was assessed for potential sutureless neurorrhaphy in PNI treatment.

Owing to its biocompatibility, biomechanical properties, and rapid self-rolling ability upon stimulation, we posited that the 4D printed rectangular gel sheets could be placed at the injury site to self-roll into a conduit *in vivo* for covering the severed ends of the resected nerve. Such an intraoperative 4D printed device could offer a marked advantage over the current technology by reducing the complexity and duration of surgeries to facilitate axonal growth and eventual regeneration and restoration of nerve function. The efficacy of 3D printed gel sheets (with and without the nanofiber coating) as intraoperative deployable implanted nerve conduits was assessed in a well-established 2 mm sciatic nerve defect model in Sprague-Dawley rats and evaluated for up to 6 weeks (Figure 4A). The animals were randomly segregated into four different groups, namely, sham, negative, and uncoated and coated 4D printed gels. No surgical damage was done to the animals in the sham group. Self-healing damage served as the negative control. The hydrogel-wrapped regions of the transected sciatic nerves six weeks post-surgery are shown in Figure 4B. No animals were lost during the test period. A combination of functional and structural assessments was analyzed to determine the success of nerve regeneration. Functional assessments such as the sciatic function index (SFI), hot plate latency, and paw withdrawal threshold were performed at specific intervals for six weeks, following which rats were sacrificed to assess the restoration of motor function in the wound-inflicted leg.

SFI measures the level of activity in the sciatic nerve. SFI was calculated by comparing the geometric representation of the damaged hind paw of an injured rat and the representation of the contralateral paw. Herein, the paw prints of the operated legs and their corresponding contralateral paws of the animals from all the groups were taken on the 1st, 15th, 30th, and 45th days (compiled in Figure 4C). In contrast to the negative control group, both the conduit-treated groups showed significant increments in SFI measurements 15th day onward post-surgery (Figure 4D). The best SFI values for both the conduit groups were observed on day 45. But among the two groups, the coated group showed a significantly increased SFI, demonstrating the superiority of coated nanofibers. (Figure 4D).

Atrophy of the gastrocnemius muscle (GA) is a common side effect of sciatic nerve damage. Muscle atrophy is reduced by the regeneration of the sciatic nerve and reinnervation of the GA. GA weight analysis was used to evaluate muscle atrophy and regeneration. After the animals were sacrificed, the gastrocnemius muscles of both hind legs were removed and weighed. The left (L) (muscle weight of operated left leg)/ Right (R) (muscle weight of normal right leg) ratio was determined for all the groups (Figure 4E). After weighing, the lowest L/R ratio was observed for the negative group, whereas it was markedly improved in the case of conduit-treated groups. No significant difference in the L/R ratio was observed among the two conduit groups (Figure 4E). Muscle atrophy and regeneration assessed by hematoxylin and eosin (H&E) staining of the GA muscle (Figure 4F) indicated that the mass, integrity, and morphology of the muscle were considerably lost in the negative group (Figures 4F ii and 4G).

These parameters were markedly improved in animals treated with the 4D printed conduits following the sciatic nerve injury (Figures 4F (iii and iv) and 4G), which were comparable to the sham group. Thus, both conduits (coated and uncoated) repaired the sciatic nerve, reinnervating the gastrocnemius muscle and reducing muscular atrophy as a result of regeneration.

The hot plate and Randall-Selitto tests were used to assess the efficacy of conduits in restoring functional motor activity. In the hot plate study, the amount of time that each animal was able to withstand the heat or wait before displaying a reaction was recorded. When the sciatic nerves of the animals are compromised, the animals have longer latency durations. This period proportionally decreases as the sciatic nerve regenerates. Figure 4H reveals that the maximum latency period was observed in the negative groups during the post-operative six weeks. The heat latency period was significantly reduced in the 4D printed conduit-treated groups, with maximum improvements observed on day 45. On the 45th day, the heat latency period for the uncoated and coated conduits was $\approx$13 s and $\approx$11 s, respectively, which were significantly lower than the negative group ($\approx$24 s) (Figure 4H). Moreover, animals in the coated conduit group showed a statistically significant reduction in the heat latency period compared to animals in the uncoated group (Figure 4H). The Randall-Selitto (Paw withdrawal threshold) test determines allodynia or neuropathic pain in the animals. Allodynia, a hypersensitivity to a pain signal, is induced by nerve damage as a result of trauma or illness. Weights provide quantifiable pressure on the injured leg in the experimental and sham-operated groups. The paw withdrawal threshold is a measure of the pressure at which an animal withdraws its paw (PWT). Figure 4I reveals that pain hypersensitivity was more successfully suppressed when the damaged sciatic nerves were treated with coated or uncoated conduits. The PWT for uncoated and coated conduits were $\approx$15 g and $\approx$16 g, respectively, on day 45 post-injury. The PWT for the negative group was $\approx$6 g. The 135% and 150% improvement observed in the uncoated and coated conduits, respectively, compared to the negative group, demonstrates the functional recovery of the resected sciatic nerve with the 4D printed nerve conduit deployed intraoperatively. However, no significant difference in PWT was observed between the uncoated and coated groups.
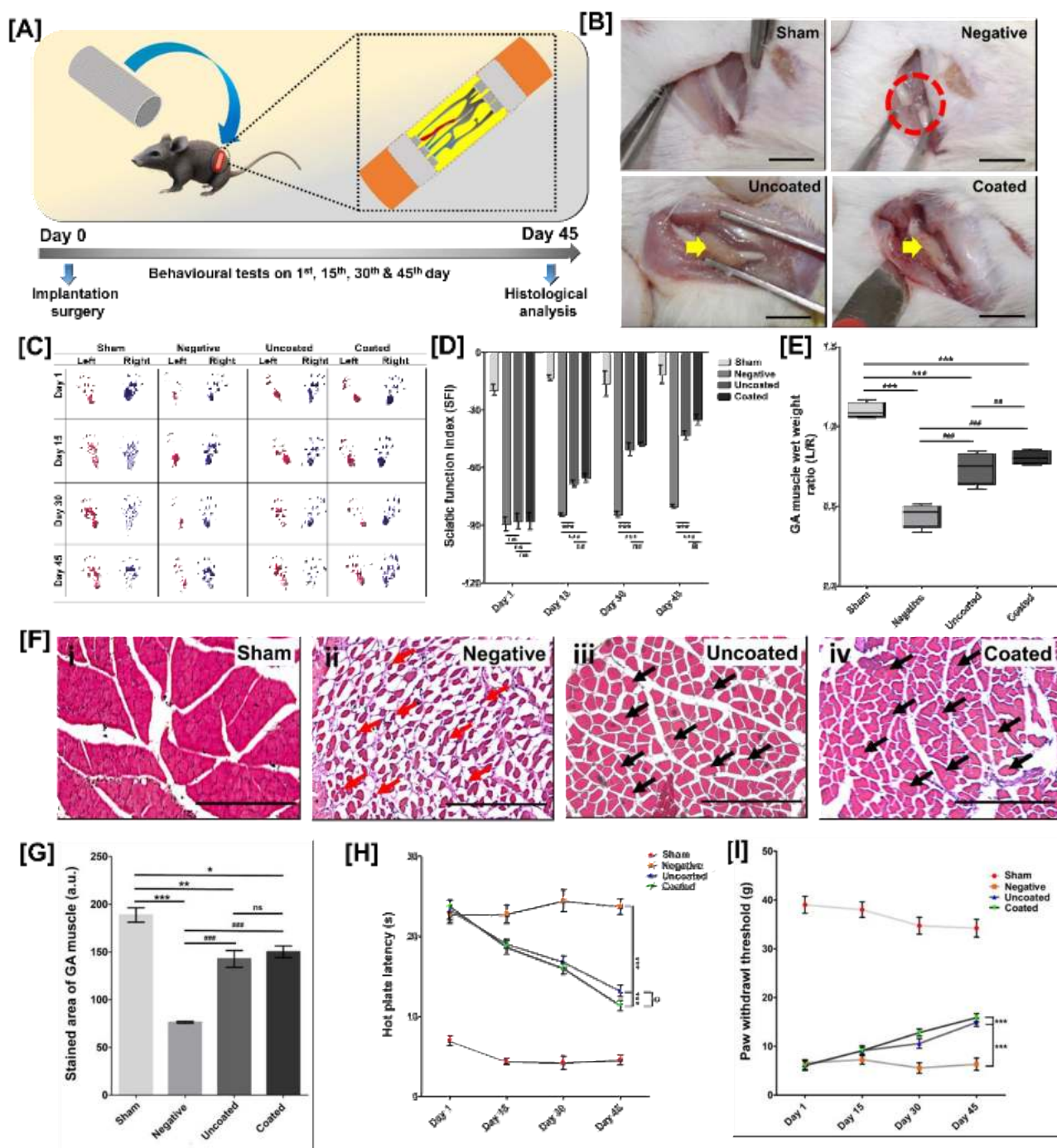
Figure 4. Direct and indirect functional assays to assess the regeneration capability of the scaffolds. [A] Schematic representation of implanting scaffolds into sciatic nerve transected SD rat model. [B] Digital images of the scaffold implantation site taken on the 45th day after the surgery in different groups (Scale bar: 1 cm). Yellow arrow indicates the area of wrapped scaffolds. Red dotted circle indicates the non-regenerated damaged nerve in the negative group. [C] Digital images of the footprints of left and right hind foot. Individual photos of left paw prints and right paw prints of animals from different groups of each time point were assembled to create the image. Red-colored paw print: Left hind leg; Blue-coloured paw print: Right hind leg. [D] Quantitative estimation of SFI of different groups at each time point. (*** denotes $p < 0.001$ vs negative; @ denotes $p < 0.05$ vs uncoated). [E] Measurements of the gastrocnemius muscle (GA) wet weight ratio (Left/Right). (*** denotes $p < 0.001$ vs sham; ### denotes $p < 0.001$ vs negative). [F] (i-iv) H&E-stained images of the GA muscle of the left hind leg

(operated limb) of rats from different experimental and sham groups. (Scale bar: 200 μm). The degenerated muscle fibrils (in the negative group) and the regenerated muscle fibrils (Uncoated and coated groups) are indicated with red and black arrows, respectively. [G] Quantification of H&E-stained area of the GA muscle. (*, **, and *** represent p <0.05, 0.01, and 0.001, respectively vs sham; ### denotes p < 0.001 vs. negative). [H] Graph representing the hot plate latency periods of the animal from different groups. (*** denotes p < 0.001 vs. negative; @ denotes p < 0.05 vs. uncoated) [I] Graph representing the paw withdrawal threshold (PWT) of the animal from different groups. (*** denotes p < 0.001 vs. negative). (ns: non-significant)

Histological investigation of the different groups revealed the success of nerve tissue regeneration. Regenerated nerve tissue was observed in the longitudinal slices of samples stained with H&E six weeks post-surgery (Figure 5(A & B)). Here, the staining of the negative control group is excluded, as no nerve connection was established between the two resected ends. H&E staining of the cross sections (Figure 5A(i-vi)) and longitudinal sections (Figure 5A(vii-ix)) in the middle of the region covered by the conduit shows that nerves and Schwann cells (SCs) were developing into the transplanted conduit, demonstrating that the injured nerves were being regenerated at the proximal end. Quantification of the H&E-stained positive area of the nerve from uncoated (Figure 5A (ii, v & viii), B) and coated conduit groups (Figure 5A (iii, vi & ix), B) confirmed more regenerating nerve fibers in the coated conduit group than in the uncoated group. The integrity of the regenerated nerve was also better in the coated group (Figure 5A (iii, vi & ix)) compared to the uncoated (Figure 5A (ii, v & viii)) groups. This enhancement in the coated group was possibly due to the biocompatible fibrous coating in the lumen of the formed tube, which mimics the natural extracellular matrix of the tissue. This fibrous coating provided the ideal environment for the Schwann cells to grow on the fibers to utilize them as tracks on which the axon could be regenerated. The findings of the H&E staining demonstrated that the sham-operated group had intact nerve fibers (Figure 5A (i, iv & vii)). These results confirm that the surface topography of tissue scaffolds played a critical and essential role in guiding the reconstruction of nerves. Furthermore, Figure 5C (i and ii) indicates that blood vessels were formed in both conduits. Blood vessels provide material exchange and enable nourishment to regenerated nerve tissues and SCs, which are essential components for nerve regeneration. Therefore, both coated and uncoated gels can aid in the healing of damaged peripheral nerves, as they promote neovascularization. Nevertheless, further research is warranted to elucidate the underlying mechanisms.
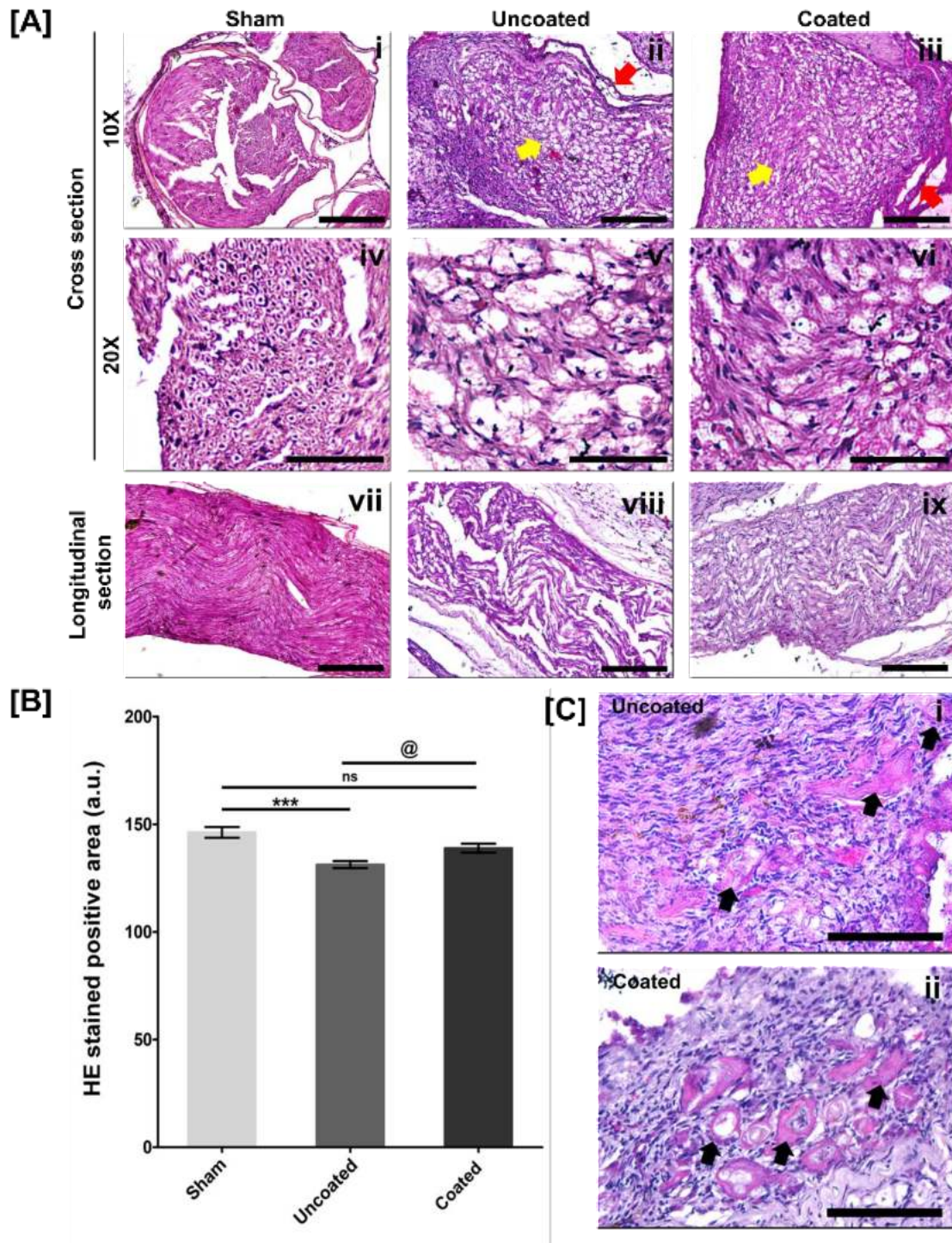
Figure 5. Assessment of the nerve regeneration potential of conduits (coated and uncoated) through histological analysis. (A) Bright-field pictures of H&E-stained transverse slices of sciatic nerves of rats belonging to various groups: (i, iv, & vii) sham, (ii, v,& viii) uncoated, and (iii, vi, & ix) coated group. Scale bar for (i-iii) & (vii-ix): 200 µm; Scale bar for (iv-vi): 50 µm. Yellow arrow indicates the regenerated nerve area; the red arrows indicate the remnant scaffolds (B) Quantification of H&E stained positive area. (*** denotes $p < 0.001$ vs. sham; @ denotes $p < 0.05$ vs uncoated). (C) H&E-stained sections of the remnant of the wrapped scaffolds in the nerve injury area. Black arrows indicated the blood vessels. Scale bar: 50 µm.

Damage to a peripheral nerve initiates a complex chain of molecular events leading to nerve regeneration. These events include Wallerian degeneration, the axonal response for phagocytosis, chromatolysis, Schwann cell proliferation, axonal growth, and target reinnervation. NF160 (Neurofilament 160), a marker for neurofilaments, is typically seen in cells or tissues of neuronal origin. Axonal regeneration requires the presence of SCs. S100β (S100 calcium-binding protein B) is a characteristic marker for SCs. Thus, both the crosssections and the longitudinal sections of the tissues were immunostained for NF-160 (green) and S100β (red), and the nuclei were counterstained with DAPI (Figure 6A). NF-160 and S-100β proteins were expressed in all the study groups, confirming the formation of myelin sheaths composed of SCs and the ingrowth of new axons in the 4D printed conduit. The mean fluorescence intensities of both NF-160 and S-100β were calculated by image processing. The highest NF-160 expression was observed in the sham group containing intact nerve fibers. Notably, the expression of NF-160 was higher in the nanofiber-coated conduits than in the uncoated conduits (Figure 6A (green panels), B). For S-100β, the sham group showed the least expression as no regeneration occurred, whereas the uncoated and coated conduits showed increased S-100β expression due to tissue regeneration (Figure 6A (red panels), C). Notably, the coated group exhibited more expression of S-100β as compared to the uncoated conduit group. Thus, the nanofibrous coating augmented the efficacy of the 4D printed nerve conduit.

Taken together, the programmable shape-changing hydrogel developed in this work was effective as a 4D printed NGC. The internal nanofibrous structure further enhanced the conduit performance by altering the gel architecture at both the macroscale and the nanoscale. The presence of gelatin in the nanofibers augments cellular interactions, as observed *in vitro*, and could enable the attachment of SCs to the conduit. Nanofibers mimic the architectures of extracellular matrices to effectively direct cell fates and functions. Therefore, this fiber-coated gel has the potential to enhance the healing capacity of large-scale lesions in thick nerves.
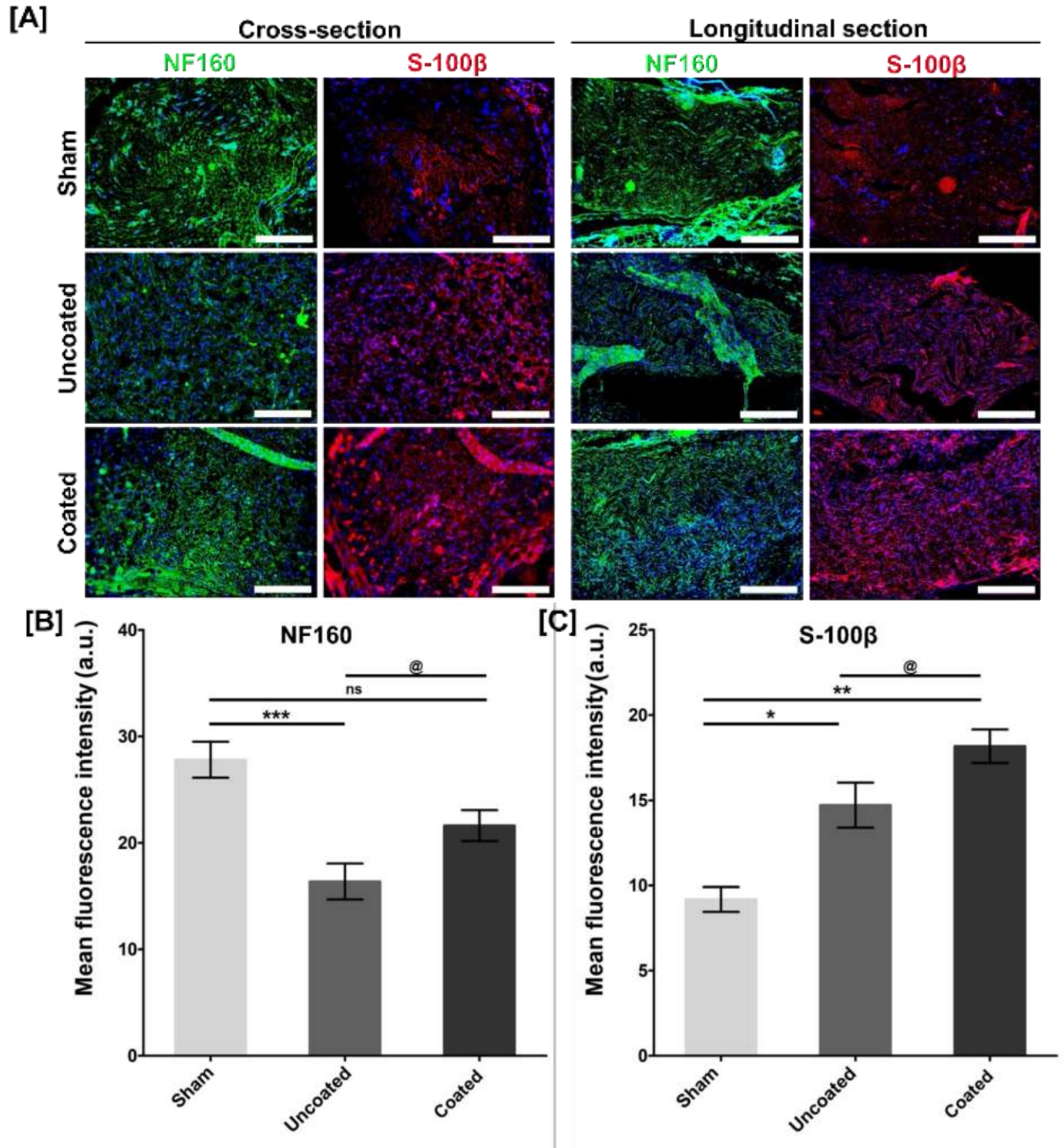
Figure 6. Assessment of the nerve regeneration potential of 4D printed conduits through histology. (A) Crosssection and longitudinal sections of sciatic nerves were stained for NF-160 (green) (a marker for neurofilaments), S-100β (red) (Schwann cell marker), and nuclei (blue). Scale bar (crosssections): 100 µm; Scale bar (longitudinal sections): 200 µm. Plots of fluorescence intensity (mean ± S.D.) for of (B) NF-160 (*** denotes $p < 0.001$ vs. sham; @ denotes $p < 0.05$ vs. uncoated) and (C) S-100β (* and ** denotes $p < 0.05$ and 0.01 respectively vs. sham; @ denotes $p < 0.05$ vs uncoated).

We focused on demonstrating the utility of the 4D printed multi-component gels for engineering NGCs, which are primarily used to bridge the gap of a severed nerve while guiding the axons to grow and avoiding scar tissue formation. So far, most research has focused on 3D printed gels, such as gelatin methacryloyl (GelMA), GelMA/PEGDA, etc., for preparing NGCs. However, 3D printed NGCs need suturing with the two nerve ends to secure the NGC at the damaged site, which requires highly skilled surgical techniques. The 4D printed NGCs developed here can be placed intraoperatively over the resected nerve ends to self-roll *in vivo,* thereby avoiding the need for suturing. This offers a marked potential clinical advancement over the current techniques. 4D printing can be leveraged to personalize the NGC to customize the diameters and lengths to match patient needs and incorporate complex design features such as branching, which would be otherwise difficult to realize.
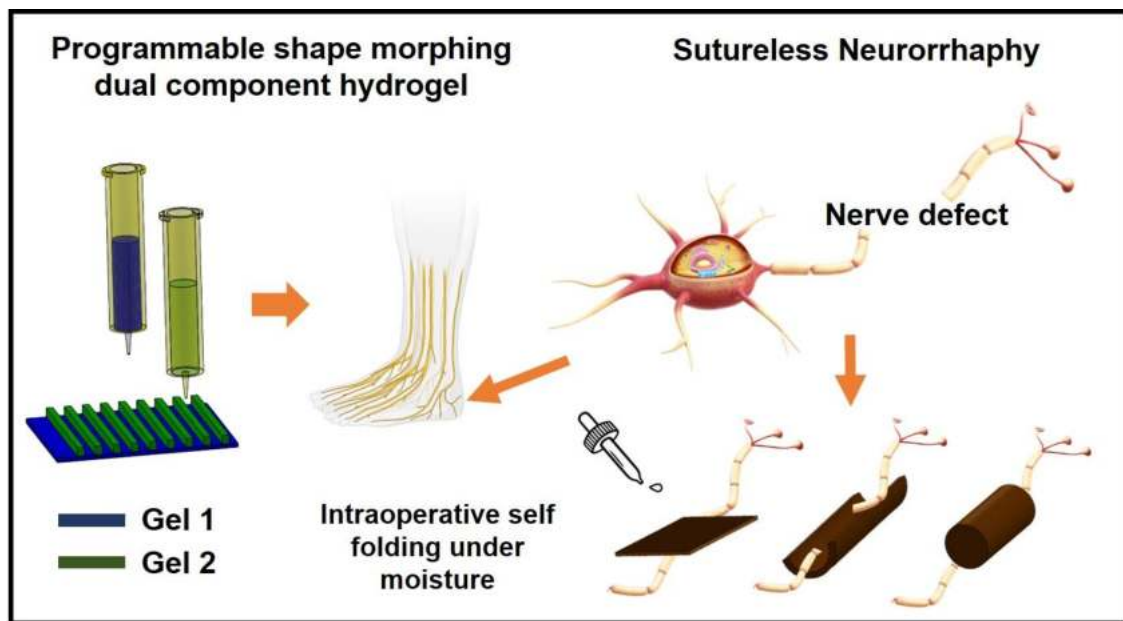

Figure 7: Schematic of dual component hydrogels being used as sutureless NGCs

On the other hand, SMPs have the unique ability to remember their original shapes and can recover back upon reheating above their glass transition temperatures. In this context, we studied the ability of SMP magnetic composite to exhibit shape recovery under remote stimulation of magnetic field and support osteogenic differentiation. As observed from Figure 8d, fluorescent images of the cells stained with the live/dead stains show that the pre-osteoblasts are viable on both PLMC and its composite with minimal cell death after 24 h. Actin and nuclear staining of the cells reveal that they are well spread and exhibit their characteristic morphology (Figure 8e). Mineral deposition is a late-stage marker of osteogenesis and can be visualized by staining with the ARS dye, which binds to calcium ions. ARS staining of the minerals deposited by the cells at 7 and 14 d demonstrates a steady increase in osteogenesis of the seeded pre-osteoblasts with time (Figure 8f). The mineral deposition was similar on both PLMC and composite scaffolds. These results demonstrate the favorable osteogenic potential of these composites, which could be partly attributed to their suitable

mechanical properties. Combined with the osteogenic potential of the PLMC-iron oxide composites, their excellent shape recovery performance through remote inductive heating near physiological temperatures make them a promising self-fitting deployable bone scaffold. The magnetic composites were printed into 3D porous scaffolds that could be potentially deployed to the site of tissue defects and triggered through inductive heating to conform to the defect size. *In vitro* and *in vivo* biocompatibility of PLMC and its composites were assessed to highlight the importance of the material systems as deployable tissue scaffolds. The composite was also demonstrated to display favorable osteogenic potential through increased mineral deposition over time.
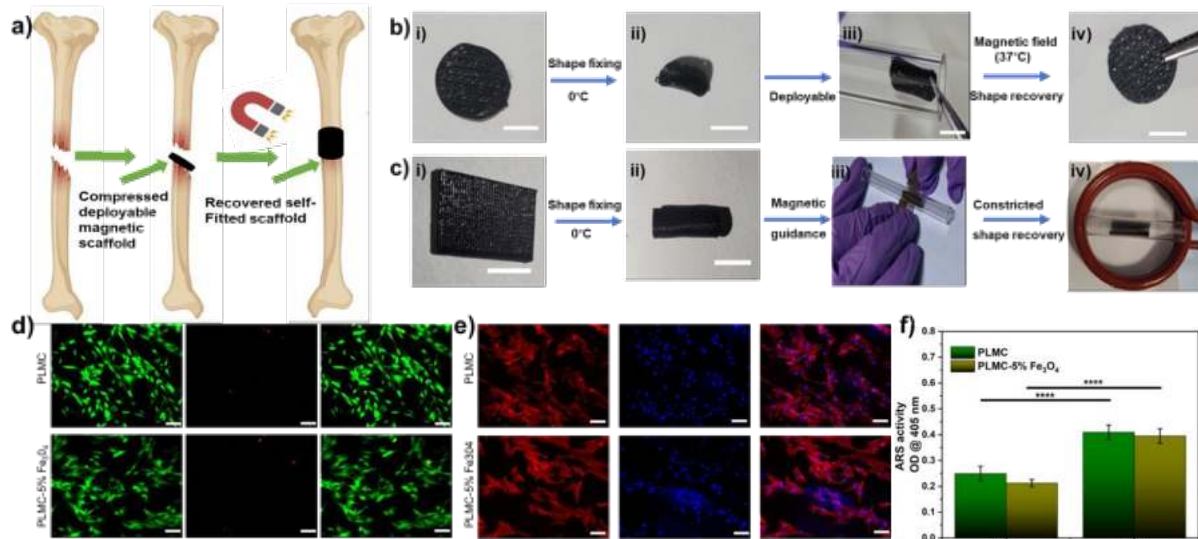

Figure 8: Shape memory magnetic composites for use as deployable bone scaffolds. a) Schematic highlighting the use of magnetic composites as deployable bone tissue scaffolds. i) Tissue defect inside the human body, ii) 3D printed composite scaffold compressed and deployed in a minimally-invasive manner, iii) Inductive heating to trigger shape recovery of the magnetic scaffold and confirm to defect shape; b) Shape recovery of 3D printed PLMC-5% Fe_3O_4 composites as deployable tissue scaffolds under alternating magnetic field. i) As-printed disc-shaped scaffold, ii) Deformed and fixed scaffold ($<T_g$), iii) Deformed scaffold able to be deployed through tube, iv) Recovered scaffold after inductive heating (Scale: 5 mm); c) Restrictive shape recovery of pre-programmed shape to original shape. i) As-printed PLMC-5% Fe_3O_4 composite, ii) Deformed and fixed shape, iii) Magnetically guided composite, and iv) Shape recovery of pre-programmed structure into original shape under alternating magnetic field. (Scale: 10 mm); d) Fluorescent images of the stained live (in green) and dead (in red) MC3T3 cells on 3D printed PLMC and composite scaffolds after 24 h post-seeding; e) Fluorescent images of the F-actin (red) and nuclei (blue) of MC3T3 cells on 3D printed PLMC and composite scaffolds 24 h post-seeding revealing the well spread morphology (Scale: 100 µm); f) ARS content indicting the minerals deposited by differentiating MC3T3 cells on PLMC and PLMC-5% Fe_3O_4 composites on day 7 and 14 (**** indicates $p<0.0001$, one-way ANOVA).

Research Impact

Taken together, these kinds of smart polymer systems combined with additive manufacturing technologies have huge potential to alter the emerging landscape of next-generation medical devices. With increasing patient burden and healthcare costs, it is imperative to find innovative solutions to pressing biomedical problems. In our study, a novel hydrogel system was shown to possess differential swelling properties and anisotropic design encoded printing which enabled it to self-roll into hollow tubes intraoperatively, without needing sutures. Current NGCs (nerve guidance conduits) are static in nature which inevitable require complex microsurgeries and sutures that cause complications. In stark contrast, the gel system in our study is dynamic and can facilitate neural regeneration without sutures.

We also show the promise of shape memory polymers (SMPs) reinforced with magnetic nanoparticles that can aid in minimally invasive procedures, and hence more patient compliant. We demonstrate the excellent shape memory behavior of the printed composites, fast shape recoveries at physiological temperatures, and potential to support bone formation. These features collectively make the composite materials a highly attractive candidate as self-fitting bone tissue scaffolds and other biomedical applications that require *in situ* triggering of shapes to conformally fill the irregular defect dimensions *in vivo*.